Jahn-Teller effects in molecules on surfaces with specific application to C_{60}

Ian D. Hands, Janette L. Dunn, Catherine S. A. Rawlinson, and Colin A. Bates

Abstract Scanning tunnelling microscopy (STM) is capable of imaging molecules adsorbed onto surfaces with sufficient resolution as to permit intramolecular features to be discerned. Therefore, imaging molecules subject to the Jahn-Teller (JT) effect could, in principle, yield valuable information about the vibronic coupling responsible for the JT effect. However, such an application is not without its complications. For example, the JT effect causes subtle, dynamic distortions of the molecule; but how will this dynamic picture be affected by the host surface? And what will actually be imaged by the rather slow STM technique? Our aim here is to present a systematic investigation of the complications inherent in JT-related STM studies, to seek out possible JT signatures in such images and to guide further imaging towards identification and quantification of JT effects in molecules on surfaces. In particular, we consider the case of surface-adsorbed C_{60} ions because of their propensity to exhibit JT effects, their STM-friendly size and because a better understanding of the vibronic effects within these ions may be important for realisation of their potential application as superconductors.

School of Physics and Astronomy, University of Nottingham, Nottingham, NG7 2RD, UK.

1 Introduction

The scanning tunnelling microscope (STM), invented by Binnig and Rohrer in the early 1980s [1, 2], has developed into a powerful tool for probing surfaces at atomic resolution. The construction and principles of operation of STMs have been amply described in the literature, and for a full account the reader is referred to any one of several texts on the subject (see e.g. [3, 4]). There are three main components to these devices: the surface under investigation, the probe 'tip', which is placed in close proximity to the surface, and the positioning and control mechanism, which acts as a means of measuring and regulating the tunnelling current between the tip and surface as their relative positions are altered. Tunnelling across the tip-surface gap occurs when a potential difference is applied. Using positive sample bias, electrons tunnel from the tip into unfilled surface states or, for molecular species, the lowest unoccupied molecular orbitals (LUMOs). Conversely, negative sample bias reverses the direction of the flow, from occupied surface states to the tip, and so an image builds up of the surface's highest occupied molecular orbitals (HOMOs).

Data is usually collected in one of two modes. In constant-height mode, the tip-surface distance is fixed and the tip moved parallel to the surface. By recording the tunnelling current as this scan proceeds, an image of the surface is generated. The other mode uses a feedback mechanism to adjust the tip-surface distance to maintain a fixed tunnelling current. In this constant-current mode, an image is produced from the height adjustments measured as the surface is scanned. In both modes, the STM can respond to molecules adsorbed onto the surface, and this produces an image of the adsorbate itself.

In 2005, Wachowiak et al. [5] used the technique to obtain remarkable images of C_{60} molecules co-deposited onto a gold surface with potassium. They found that K doping produced discrete domains corresponding to monolayers with stoichiometries K_3C_{60} and K_4C_{60}. Furthermore, the latter were electrically insulating whilst the former were conducting in nature. This behaviour was attributed to the Jahn-Teller (JT) effect. Wachowiak et al. went even further and suggested that their images could be explained by assuming the C_{60}^{4-} ions in the insulating phase had been distorted by the JT effect into species of D_{2h} symmetry. The C_{60}^{3-} ions in the conducting phase, however, were not showing signs of a JT effect of any kind, according to their interpretation.

These results are extremely interesting in light of the discovery made in 1991 that alkali-doped A_3C_{60} compounds exhibit superconductivity with transition temperatures $T_c \sim$18–28 K [6, 7]. Since then, these fullerides have been the subject of great interest and other compounds with even higher T_c values have been synthesized [8]. Superconductivity in fullerides [9] may, in part, be due to vibronic coupling and so observation of the JT effect in fulleride ions in various charge states using STM is particularly attractive. If correctly interpreted, the STM results should permit quantitative data on the degree of coupling in these ions to be ascertained. This, in turn, should

allow an assessment to be made of the contribution vibronic coupling makes to superconductivity in these compounds.

It is apparent, therefore, that methods of interpreting the ways in which the JT effect affects the images produced using tunnelling microscopy need to be developed. Currently, it would seem, experiment outstrips theoretical work as little appears to have been written about the JT effect in a specifically surface-adsorbed environment. There may be good reasons for this. The JT effect is a rather subtle effect. At its core, is a spontaneous loss of symmetry driven by the ensuant lowering of the energy of the system. However, there is always more than one way in which this JT distortion can be achieved. Subsequently, quantum mechanical tunnelling between these differently distorted forms restores the original symmetry provided we consider a sufficiently long period of time. How will this dynamic picture be affected by the presence of a surface? Are there other complications that need to be considered? One of our aims here is to give recognition to some of the problems that may complicate observation of the JT effect via STM.

In Sect. 2, we give a general discussion of some of the problems that need to be considered when a JT-active molecule is adsorbed onto a surface, with specific application to C_{60}. Then, in Sect. 3 we give an overview of the C_{60}-related STM images that have been published in the literature. Some of these images can be readily accounted for without invoking a JT effect; this is the main thrust of Sect. 4. In Sect. 5, we try to concentrate on what features could be produced in an STM image by the JT effect. Finally, in Sect. 6 we draw our considerations to an end with a summary of our most important findings.

2 General considerations

For an isolated system, treatment of the intramolecular Jahn-Teller effect is relatively simple. As the system is isolated, we may ignore molecular rotation and consider a molecule-fixed coordinate system. Within this frame of reference, the electronic and vibrational states can be formulated in terms of the irreducible representations (irreps) of the reference configuration. Overall, the system Hamiltonian is generally written in the form

$$\mathcal{H} = \mathcal{H}_0 + \mathcal{H}_{\rm JT} \ , \tag{1}$$

where $\mathcal{H}_{\rm JT}$ constitutes the JT interaction Hamiltonian and $\mathcal{H}_0$ is the vibrational Hamiltonian.

Now consider a system that is not isolated but interacts with a surface. We now need to add an additional term $\mathcal{H}_{\rm S}$ to Eq. (1) that represents the interaction with the surface. In general, the surface interaction will lead to distortion of the system and so $\mathcal{H}_{\rm S}$ could be written as an expansion in terms

of the normal modes Q^Γ of the system, such that

$$\mathcal{H}_\mathrm{S} = \mathcal{H}_\mathrm{S}^{(0)} + \sum_{\Gamma,\gamma} W_\gamma^\Gamma Q_\gamma^\Gamma \ . \tag{2}$$

In this expression, $\mathcal{H}_\mathrm{S}^{(0)}$ represents a purely electronic interaction between an undistorted system and the surface, and W^Γ are electronic operators determining the interaction between a vibration (irrep Γ, component γ) and the surface. These latter operators must therefore have transformation properties dictated by the symmetry of both the adsorbed molecule and the surface. The form of Eq. (2) is suggestive of the standard method by which JT theory is developed, and this may be a desirable approach for future work. As a first approximation, however, we ignore the additional complication of surface-induced distortion and concentrate on the zeroth order term $\mathcal{H}_\mathrm{S}^{(0)}$.

Unlike the isolated molecule case, the presence of a surface defines a reference set of coordinates so that molecular orientation cannot be ignored. In other words, the interaction between the molecule and the surface depends on the orientation of the molecule with respect to the surface so that

$$\mathcal{H}_\mathrm{S}^{(0)} = \mathcal{H}_\mathrm{S}^{(0)}\left(\boldsymbol{R}, \boldsymbol{\Omega}\right) \ , \tag{3}$$

with $\boldsymbol{R}$ a vector specifying the location of the molecule with respect to a surface-fixed frame and $\boldsymbol{\Omega} = (\phi, \theta, \psi)$ a set of Euler angles specifying its orientation. For C_{60}, the interaction will therefore depend on whether a pentagonal, hexagonal, or other characteristic site (e.g. a double or single bond, or even a single atom) is oriented towards the surface *and* the symmetry of the surface involved. For example, consider a scenario in which a pentagonal face of the C_{60} molecule binds preferentially to a surface of C_{6v} symmetry, as in Fig. 1. The interaction energy in this case will clearly depend on the separation between the C_{60} and the surface and an azimuthal angle ϕ_a defined as the angle between a surface-fixed (σ_d) and molecule-fixed (σ_v) mirror plane. In this case, the surface interaction is subject to the condition $\mathcal{H}_\mathrm{S}^{(0)}\left(Z, \phi_a + \pi/3\right) = \mathcal{H}_\mathrm{S}^{(0)}\left(Z, \phi_a\right)$ and six local minima in the potential energy surface (PES) are to be expected.

For a very strong interaction, the freedom of the molecule to rotate around the surface normal will be diminished, perhaps to the point where the molecule will be 'locked' into a particular potential well. For weaker interactions, the system can tunnel from one well to another making the system dynamic and restoring a higher degree of symmetry to the system. These possibilities are analogous to the concept of static vs. dynamic JT effects but they will be present even if the adsorbed molecule is not JT-active. Note that if this system happened to be in a dynamic state, and was subsequently observed via STM, then the molecule's fivefold symmetry would not be apparent, even though it must still be present as the molecule is rigid.

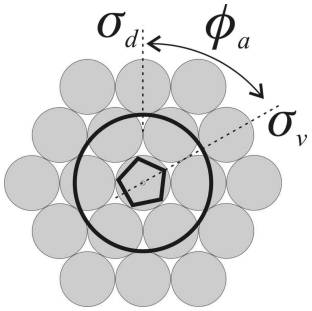

Fig. 1 Plan view of a C_{60} molecule (black ring) on a hexagonal surface. In this figure, the C_{60} is chosen to be on top of a surface atom with a five-membered ring (black pentagon) directed towards that atom. The PES depends on their relative orientations as given by the azimuthal angle ϕ_a.

The foregoing discussion raises the question of temperature. At low temperatures, the C_{60}-surface interaction has a greater ability to lock the adsorbed molecule into a fixed orientation. Therefore, intramolecular detail is most likely to be apparent in STM images at low temperatures. Raising the temperature will give greater freedom for the molecule to rotate about the surface Z-axis and therefore the STM image will be more likely to show features indicative of the substrate symmetry. For example, in Fig. 1 the STM image of the molecule would be expected to have sixfold symmetry. Adsorption at an interstitial site could similarly result in STM images having threefold symmetry if the rotational freedom is great enough. At even higher temperatures, full rotational freedom could result in spherically symmetric STM images. In this respect, what constitutes a 'high' or 'low' temperature will depend on the strength of interaction with the surface. Therefore, it is possible that for a given temperature and surface, STM images of individual C_{60} molecules could appear different simply because they are adsorbed at sites with different degrees of C_{60}-surface interaction. We shall look more closely at the effect of temperature later in Sect. 2.1.

Another problem encountered due to the presence of the surface is that of charge transfer (CT). This is especially so in light of the fact that C_{60} is a good electron acceptor with an electron affinity of 2.689 eV [10]. Thus, CT is likely to occur whenever C_{60} is adsorbed onto a metallic surface. The donated electrons will be accommodated in the T_{1u} orbitals of C_{60}, and this will render them susceptible to a JT effect. In Sect. 2.2, we tabulate some values for the CT found or calculated for some surfaces commonly used in STM.

Whenever CT occurs, we can expect it to engender a strong interaction with the surface as the ions will interact strongly with their cationic counterimages induced within the metal. Subsequently, the LUMO could be strongly split due to the presence of a metallic surface alone. Of course, any such splitting will be governed by the symmetry of the interaction as well. Multiple occupancy of the T_{1u} orbitals also brings with it the problem of electron-electron interactions. These issues are dealt with more thoroughly in Sect. 2.3. Fi-

nally, we shall also give a brief discussion in Sect. 2.4 of another surface related problem, viz. the formation of monolayers.

2.1 Time-scales and temperature

Existing STM techniques are undoubtedly slow, with the fastest machines having a millisecond time resolution. This has lead to attempts to develop techniques of improving temporal resolution 100-fold [11]. However, even with the limited time resolution currently available there have been some useful time-dependent STM studies. For example, compilation of several series of static images into video clips has provided valuable insight into catalytic activity and diffusion of molecules on surfaces [12]. A typical, nominally 'fast', scan rate used in the latter work suggests that an area $140 \times 140\,\text{Å}^2$ can be imaged in $\sim$13 s. C_{60} has a diameter of $\sim$7 Å, which gives a dwell time per C_{60} of roughly 33 ms. This limitation arises from the electronics used and not the tunnelling process [11]. We can therefore safely assume that any motion faster than this is not currently detected in STM experiments. In fact, as electrons injected or removed by the STM tip will create excitations in the vibronic states, tunnelling could be induced by the STM tip itself. Hence JT tunnelling is likely to remain fast compared to STM measurements, even with potential future improvements in electronics. Nevertheless, we can proceed to estimate upper limits on survival times of static distortions by ignoring the effect of the STM measurement process itself.

Many of the STM images involving C_{60} are obtained at low temperatures ($\sim$5 K). It is pertinent to consider what the time-scales are for typical molecular motions at these low temperatures. Repp et al. [13] recorded STM images of copper clusters, comprising 1–3 atoms on a Cu(111) surface, at a variety of temperatures. The copper dimer appears as a circular object via STM, even at 5–7 K. The dimer is so imaged because the copper atoms have enough energy to diffuse locally between face-centred cubic (fcc) and hexagonal close-packed (hcp) sites. The authors measured the rate at which fcc-fcc dimers converted to fcc-hcp dimers as a function of temperature. Above $\sim$6 K, the measured conversion rate r conforms to the classical Arrhenius equation,

$$r = r_\infty \exp(-E_\text{b}/kT) \tag{4}$$

where E_b is the barrier to conversion and r_∞ is the 'attempt frequency'. From the experiments, it was found that $r_\infty = 8 \times 10^{11\pm0.5}\,\text{s}^{-1}$ and the barrier to diffusion was $E_\text{b} = 18 \pm 3$ meV. At 6 K, this implies a conversion rate of $6.1 \times 10^{-4}\,\text{s}^{-1}$. Therefore, the time taken to jump from one configuration to another is $\sim 10^3$ s. This slow process would obviously be easy to measure using STM.

At 7 K, the conversion rate has increased 100-fold to $\sim 0.1\,\mathrm{s}^{-1}$, so that it takes about 10 s to hop between configurations. Even the fastest scanners take about this time to capture their data and so slower systems could be expected to see the dimer as a circular blur. It is interesting that a relatively modest change in temperature of 1 K should make the difference between observation of Cu_2 as a 'dumb-bell' or something more isotropic. Clearly, even for 'small' barriers, a small temperature change can have a significant effect on the STM image.

Treating the Cu_2 dimer as a rigid rotor (bond length ~ 2.6 Å), results in a moment of inertia of $I_{Cu_2} = 3.6 \times 10^{-45}\,\mathrm{kg\,m^2}$, corresponding to a rotational constant of $B_{Cu_2} = 1.0 \times 10^{-2}\,\mathrm{meV}$. A direct calculation of the rotational energy gives a mean value of $\langle E_J \rangle = 0.52\,\mathrm{meV}$ at 6 K. If we equate this with the kinetic energy for a classical rotor ($\frac{1}{2} I\omega^2$), we get a measure of the mean angular velocity ω. We suppose that an attempt to cross the barrier has occurred if the dimer rotates by the angle sufficient to take the dimer from a fcc-fcc well minimum to a barrier maximum. Simple geometry shows the angle to be 16.1°, which combines with the rotation speed to yield $r_\infty(Cu_2) = 7.8 \times 10^{11}\,\mathrm{s}^{-1}$. This is in very good agreement with the observed rate.

We can repeat this rough calculation for C_{60} which has a much larger moment of inertia than the dimer ($1.0 \times 10^{-43}\,\mathrm{kg\,m^2}$). At 6 K, we estimate the angular velocity to be $\omega_{C_{60}} = 4.1 \times 10^{10}\,\mathrm{rad\,s}^{-1}$, leading to an estimated attempt frequency of $r_\infty(C_{60}) = 7.8 \times 10^{10}\,\mathrm{s}^{-1}$. This is 10 times smaller than in the copper dimer case. At this stage, we can use Eq. (4) to calculate a critical barrier height E_{crit} for low temperature STM. For $r \sim 10^{-3}\,\mathrm{s}^{-1}$ and $kT = 0.52\,\mathrm{meV}$ (6 K), we find

$$E_{\mathrm{crit}} \sim 17\,\mathrm{meV}\ . \tag{5}$$

If the barrier energy is lower than this critical value, rotational motion will be fast at 6 K and the STM image will be smeared out and STM simulations will need to include time averaging. If the barrier is larger, then the image may have threefold or sixfold symmetry depending on the energies of the local minima.

Repeating the above steps for a general temperature yields

$$E_{\mathrm{crit}} \sim \frac{1}{2} kT\,(\ln kT + 64.6) \quad (E_{\mathrm{crit}}, kT \text{ in meV})\ . \tag{6}$$

(This assumes the attempt frequency has a temperature dependence. If instead we assume that $r_\infty = 7.8 \times 10^{10}\,\mathrm{s}^{-1}$ irrespective of temperature, then Eq. (6) becomes $E_{\mathrm{crit}} \sim 32.0\,kT$.)

A recent density functional theory (DFT) study [14] of C_{60} on Cu(111) indicates that the adsorbate is most energetically stable when localized over a hcp site (although the fcc site is only 20 meV higher in energy). A barrier to rotation of 300 meV is predicted. According to Eq. (5), this barrier would

be sufficient to prevent rotation on an STM time-scale at 6 K. However, at room temperature Eq. (6) suggests that the critical barrier should be nearer to 855 meV, and so rotation may not be suppressed.

The overall conclusion is that provided $T \sim 7$–10 K we should be fairly confident that C_{60} adsorbs onto metallic substrates with a fixed orientation, with little rotational freedom. Of course, the observation of intramolecular detail in STM is a reliable indicator that rotation has been suppressed to some degree. However, as we have tried to emphasise, even this observation may not mean that motion has been completely stifled.

2.2 Charge transfer

As C_{60} has a high electron affinity (2.689 eV [10]), charge transfer will be a distinct possibility whenever C_{60} is adsorbed onto a metallic surface. The T_{1u} LUMO of C_{60} can accept up to six electrons, but there is no reason to believe, a priori, that such a large CT should be sustainable on a metallic surface. In fact, a calculation by Burstein et al. [15] suggests that a maximum CT of two electrons to each C_{60} is to be expected, regardless of the work function of the metal.

The problem of charge transfer from metals to C_{60} molecules adsorbed on their surfaces has been addressed by several authors using both experimental [16, 17, 18, 19] and theoretical approaches [15, 20, 21]. A (non-exhaustive) summary of their results is given in Table 1, which also lists the work functions of the substrates involved. As can been seen from the table, a larger CT generally correlates with a smaller work function, as might be expected. It is also interesting that even relatively inert metals such as gold are thought to transfer ~ 1 electron to the C_{60}. Also note that the tabulated CT values appear to support Burstein's calculation of a maximum CT of $2\,e/C_{60}$ [15].

Charge transfer to the C_{60} molecule will lead to occupation of the T_{1u} LUMO of the neutral molecule and this should be sufficient to render the molecule liable to distortion via the JT effect. Therefore, if it is possible to observe signatures of the JT effect using STM, then these signatures should be apparent in even the simplest experiments involving C_{60} on metal surfaces, provided CT occurs.

In a certain sense, the simple C_{60}–metal system provides the 'purest' test cases in which to seek the JT effect. Additional doping by co-deposition of, say, potassium has the benefit of creating more highly charged ions, e.g. C_{60}^{3-}, which may be subject to stronger vibronic coupling. This could increase the likelihood of observing the JT effect via STM, but there is also the possibility that the dopant may have other hidden effects that could unwittingly affect the image and lead to erroneous conclusions being drawn.

As a final comment on this aspect of the problem, it is worth mentioning that even in situations where C_{60} can be effectively decoupled from the

Table 1 A selection of substrate work functions and the charge transfer that occurs from them to adsorbed C_{60} molecules. Numbers in italic font are calculated values and references are in square brackets.

Surface	Work function[a] (eV)	Charge transfer[b] (e/C_{60})
Ag(polycr.)	4.3 ± 0.1 [18]	1.7 ± 0.2 [18]
Ag(001)	4.64	1.7 ± 0.08 [19]
Ag(110)	4.52	
Ag(111)	4.74	0.75 [17]
Au(polycr.)	5.2 ± 0.1 [18]	1.0 ± 0.2 [18]
Au(110)	5.37	1 ± 1 [16]
Au(111)	5.31	
Cu(polycr.)	4.5 ± 0.1 [18]	1.8 ± 0.2 [18]
Cu(111)	4.94	*0.8* [14], 1.6 [22]
Pt(110)	5.84	*−0.07* [21]
Rh(111)	5.4 [23]	$\ll 1$ [24]
Si(100)–(2×1)	4.91	0 [25]
Si(111)–(7×7)	4.60	(0.7 to 3)[c] ± 1 [25]

[a] From [26], unless otherwise referenced.
[b] Mean number of electrons transferred from the surface to each C_{60}.
[c] Dependent on coverage.

surface, JT effects may still be apparent. This is because of the tunnelling nature of STM which necessarily involves electron transportation through the molecule. Thus, vibronic signatures have been recently recorded in differential tunnelling-current vs. bias ($\mathrm{d}I/\mathrm{d}V$) spectra in single C_{60} molecules supported upon 1,3,5,7-tetraphenyladamantane nanostructures on a gold substrate [27].

2.3 Surface interactions and symmetry

There are 17 two-dimensional space groups arising from five Bravais nets associated with translation over a surface [28]. A C_{60} molecule adsorbed onto a surface will therefore be subject to a local symmetry belonging to one of ten possible site symmetries: C_{6v}, C_6, C_{4v}, C_4, C_{3v}, C_3, C_{2v}, C_2, C_s, and C_1. None of these site groups support triply degenerate irreps and so the T_{1u} LUMO will be split whenever C_{60} is adsorbed onto a surface. If the symmetry is C_3 or higher (i.e. one of the first six symmetries in the list above), the LUMO will split into a doublet and a singlet. If the symmetry is C_{2v} or lower, it will split into three singlets. C_{60} on a surface will therefore be subject to a Jahn-Teller effect involving one of these states, or to a pseudo-JT effect involving more than one of these states.

Consider the case of C_{60} adsorbed onto the (111) surface of a fcc lattice as exemplified by Au(111), Ag(111) and Cu(111), surfaces that are commonly used in STM studies. These surfaces belong to the C_{3v} factor group, which

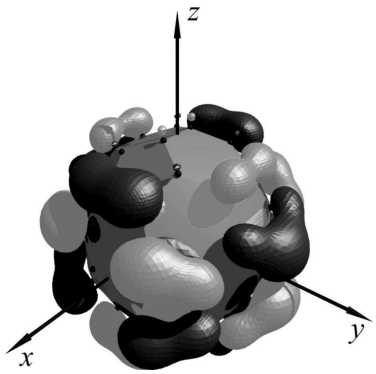

Fig. 2 Electron distribution associated with the T_{1uz} orbital. The lighter lobes correspond to wave functions with a positive sign. The other orbitals are identical apart from their orientation (obtained by cyclic permutation of the axes.)

has irreps A_1, A_2 and E. When the C_{60} molecule is oriented so that it is subject to this C_{3v} environment, the correlations $\{T_{1u}, T_{2u}\} \rightarrow \{A_1 + E\}$ and $\{H_u\} \rightarrow \{A_2 + 2E\}$ apply. Therefore, the T_{1u} LUMO will be split into two sets of molecular orbitals. Examination of the distributions associated with the T_{1u} orbitals shows that the electrons occupy an 'equatorial' belt around the molecule with respect to the associated axis. For example, Fig. 2 shows the T_{1uz} orbital in a frame in which the Cartesian axes pass through carbon-carbon double bonds. This suggests that upon adsorption in a C_{3v} environment, the A_1 orbital should be associated with the direction normal to the surface and the degenerate E orbitals should be associated with two orthogonal directions parallel to the surface.

The energy difference $\Delta_S = E_{A_1} - E_E$ between the (A_1, E) pair is determined by the interaction with the surface, and the sign of Δ_S could be positive or negative. In general, we need to consider three cases, referred to as $p^1(\equiv p^5)$, $p^2(\equiv p^4)$, and p^3, corresponding to the number of electrons which would occupy the unsplit p-like T_{1u} orbital in the absence of surface interaction. However, we must include electrons transferred as a result of charge transfer to reflect the C_{60} species that is present on the substrate. Thus, the p^1 case accounts for a nominally C_{60}^- ion (or C_{60}^{5-} ion using electron-hole symmetry). This situation could arise if C_{60} is adsorbed onto a metal which subsequently donates one electron to it, or if an adsorbed but still neutral C_{60} molecule is chemically doped using an adsorbate such as an alkali metal.

Like the JT effect, the surface interaction will tend to favour low spin configurations. On the other hand, electron-electron Coulombic repulsion will favour high spin arrangements. Therefore, we need to derive correlation diagrams for the electronic interactions that will arise in each of the three p^n cases. In Fig. 3, we show the simple term splitting diagram for the p^1 case with C_{3v} surface splitting. The central part of the diagram represents the case of a free C_{60}^- ion and the right hand side shows the behaviour to be expected if a positive surface splitting occurs. Conversely, the left hand side applies to negative splitting. The same diagram applies to the p^5 case provided we reflect the diagram horizontally (or change the sign of Δ_S) because of

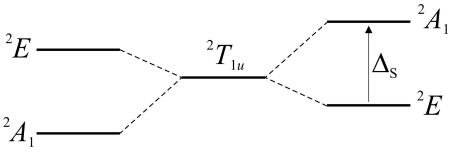

Fig. 3 Correlation diagram for p^1 (C_{60}^-) or p^5 (C_{60}^{5-}). The central term is that appropriate to free icosahedral ions, the right hand side for positive C_{3v} surface splitting $\Delta_S > 0$, and the left hand side for equivalent negative splitting.

electron-hole symmetry. Thus, a p^5 configuration with positive splitting gives rise to a $^2A_1$ ground state.

The same format used in Fig. 3 is adopted in the multielectron cases shown in Figs. 4 and 5. In the absence of surface interaction (centre of each diagram), electron-electron repulsion gives rise to three possible electronic terms, whose separations are determined by an exchange parameter J [29]. For p^2, the terms are $\{^3T_{1g}, ^1H_g, ^1A_g\}$ with energies $\{-J, J, 4J\}$, and for p^3 the terms are $\{^4A_u, ^2H_u, ^2T_{1u}\}$ with energies $\{-3J, 0, 2J\}$. Calculated values of J vary considerably, with the actual value likely to be somewhere in the range 30–110 meV (see [29] and references therein). These terms will be split if the surface interaction is included as a perturbation, producing (in C_{3v} surface symmetry) singly and doubly degenerate orbitals as shown to the left and right of the centre of the diagrams. Note that the splitting shown here has only qualitative significance. On the extreme left and right of Figs. 4 and 5, the configurations that exist in the case of infinitely strong surface interaction are shown. For a strong but finite interaction, these configurations will be split by the electron-electron interaction which is now considered to be a weak perturbation.

The term diagrams in Figs. 3–5 allow the expected pattern of electronic excitation to be predicted for a surface splitting of C_{3v} symmetry, provided the strength of the interaction with the surface is known. Conversely, we might hope to deduce the magnitude of the surface interaction from knowledge of excitation spectra, if these can be obtained from adsorbates.

In this section, we have considered the specific example of a C_{60} ion subject to a C_{3v} surface splitting. Analysis for lower symmetries can be performed in a similar way, where for all symmetries C_3 or higher there is still a doublet and a singlet, and for symmetries of C_{2v} or lower there will be three singlets.

2.4 C_{60} monolayers

A further complication to the picture already presented arises when the concentration of C_{60} molecules on the surface increases. Clearly, the greater the surface concentration, the greater the importance of intermolecular in-

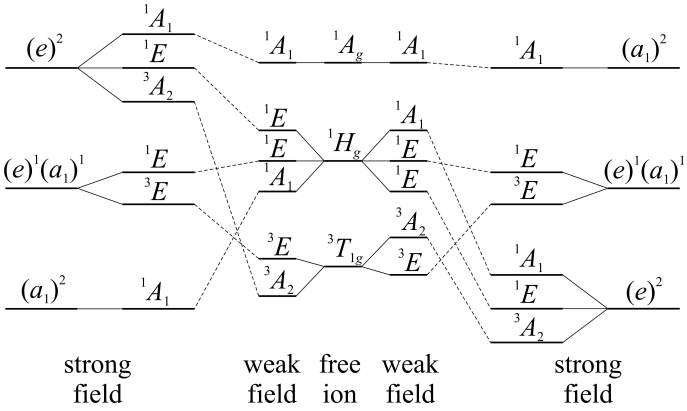

Fig. 4 Correlation diagram for p^2 (C_{60}^{2-}) or p^4 (C_{60}^{4-}) with C_{3v} surface splitting. Terms arising from positive splitting are on the right and from negative splitting on the left with magnitudes that increase with distance from the centre of the figure. At the extreme edges of the diagram, the strong field (i.e. strong surface interaction) configurations are shown. The order of the terms for the free ion is taken from ab initio calculations [29]. In C_{3v} symmetry, only $A_1 \leftrightarrow A_2$ transitions are not allowed.

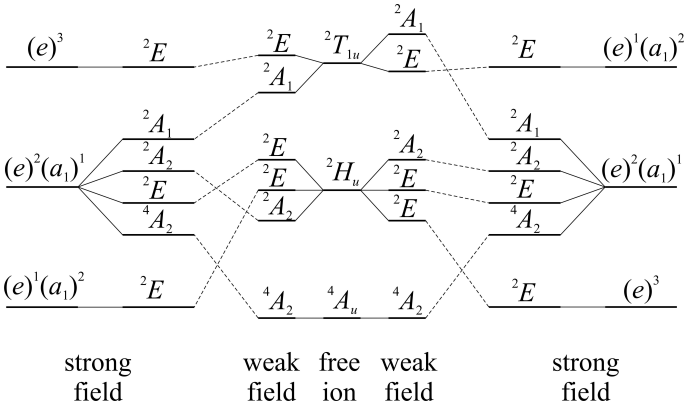

Fig. 5 Correlation diagram for p^3 (C_{60}^{3-}) with C_{3v} surface splitting. The structure of the diagram is as in Fig. 4 and once again the order of the terms for the free ion is taken from ab initio calculations [29].

teractions between adjacent C_{60} units. Of particular importance is when the concentration corresponds to monolayer (ML) coverage. Due to their sphericity, C_{60} MLs adopt close-packing arrangements. This, in itself, exposes each C_{60} to a local environment that is approximately C_{6v} or C_{3v} in symmetry. As before, this interaction will remove the degeneracy of the T_{1u} LUMO. In this case, however, we might expect the sign of the splitting to be opposite to that caused by the surface.

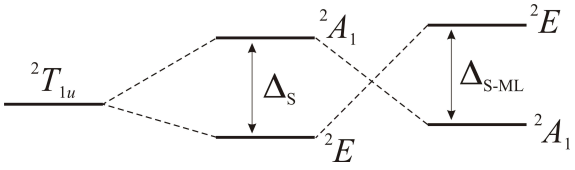

Fig. 6 Net splitting Δ_{S-ML} of the T_{1u} LUMO in C_{60} due to a C_{3v} interaction with a surface and subsequent monolayer formation.

Referring to Fig. 2, let us suppose the surface is located in the negative z-direction. Electrons located in the T_{1uz} orbital are in an equatorial location and are therefore ideally located to interact with neighbouring C_{60} molecules, but not with the surface. Conversely, electrons in the T_{1ux} and T_{1uy} orbitals are in equatorial belts that point towards the surface. These, therefore, are expected to interact more strongly with the surface but be less inclined to interact with neighbours. In some respects, then, ML formation negates the surface interaction, as shown in Fig. 6. Even a very strong surface interaction could be cancelled by strong interactions within the monolayer. There may be evidence in the literature for this splitting cancellation. Photoemission spectra obtained from an increasingly K-doped monolayer of C_{60} on Ag(111) shows a triply degenerate LUMO progressively filling with electrons, but no splitting [17]. In contrast, a study [30] using STM techniques to sequentially K-dope an *individual* C_{60} molecule on a Ag(001) surface showed a clear splitting in the $\mathrm{d}I/\mathrm{d}V$ spectrum of the undoped C_{60}, as shown in Fig. 7. This splitting could be an indication that the interaction of a single C_{60} molecule with the silver surface is non-zero, i.e. $\Delta_S \neq 0$.

Provided the monolayer interaction splits the LUMO into a singlet and a doublet, and the surface does the same, then there will be an effective, overall splitting which we call Δ_{S-ML}. The correlation diagrams in Figs. 3–5, therefore, will still be applicable. On the other hand, it is clearly conceivable that the combination of all the interactions affecting any particular C_{60} may completely lift the degeneracy of the LUMO. In this case, STM images matching individual components of the LUMO may be obtainable depending on the bias used. Thus, STM should provide an ideal technique for experimentally determining the order and energy of any splitting present. This, in turn, should provide evidence for the local symmetry experienced by the molecule on the surface.

3 STM imaging of fullerenes: An overview

The first paper to report an STM image of C_{60} molecules on a surface [of Au(111)] was published in 1990 [31], where the tendency of C_{60} to form hexagonally close-packed monolayers is apparent. In this early work, the fullerene molecules look little more than spherical blobs. Since then refinements to the STM technique, including the ability to record images at liquid helium

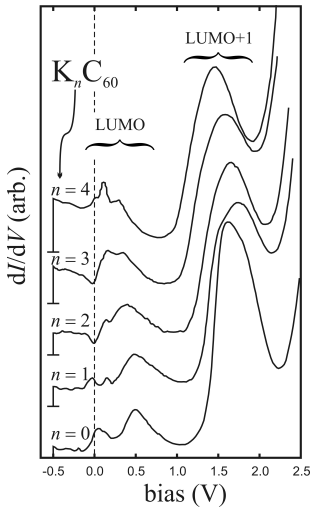

Fig. 7 Tunnelling spectra from a single C_{60} molecule on Ag(001) subject to progressive K-doping. The spectra have been off-set to improve clarity. The LUMO appears to be split differently in each trace; possibly due to the influence of K^+ ions. Note, however, that the undoped trace also shows signs of splitting, implying $\Delta_S \neq 0$. Reprinted figure with permission from R Yamachika, M Grobis, A Wachowiak and MF Crommie, Science **304**, 281 (2004) [30]. Copyright (2004) by The American Association for the Advancement of Science.

temperatures, have greatly increased the quality of the images and the data therein. Subsequently, a large body of knowledge has been accumulated. It is not our purpose to give a thorough review of this body here. Instead, we will pick out a limited number of the most relevant papers in order to illustrate the most important features that have been observed. Subsequently, we will attempt to rationalise these features using theoretical simulations. A more general review of STM imaging as applied to fullerenes up to 1996 can be found in Ref. [32].

One of the earliest works showing clear evidence of intramolecular detail within individual C_{60} units is that of Motai et al. [33], as shown in Fig. 8. These images are striking because it strongly suggests that the C_{60} adsorbs to the copper surface with a hexagonal face pointing downwards and that each C_{60} cooperatively aligns itself with its neighbours. It also exemplifies the tendency of C_{60} to form close-packed monolayers. These bias-dependent images can be explained in terms of the electron distributions associated with the LUMO and HOMO of C_{60} [34], as we illustrate in Sect. 4.2.

Further internal electronic structure arising from the HOMO orbitals was observed by Tsuchie et al. [35], who studied C_{60} monolayers on a Si(111)–$\sqrt{3} \times \sqrt{3}$–Ag surface at room temperature and at 60 K using a fixed sample bias of -2 V. Fig. 9 shows the images obtained from a plain C_{60} monolayer and one that has been doped with potassium. It is readily seen that doping has a significant effect on the resulting images. The reason why doping has such a marked effect on the image does not seem to have been explained or thoroughly investigated. One would expect K-doping to alter the energies of the imaged orbitals as a result of charge transfer to the fullerene cage. This

would bring different orbitals 'into view' at the fixed bias used. Another possibility is that doping affects the molecule's electronic structure to such an extent that the molecule rotates into a different orientation upon doping. This could, in fact, be evidenced by Fig. 9 as the structures shown in Fig. 9(a) are consistent with molecules oriented with a C_2 rotational axis perpendicular to the surface, whereas this does not appear to be the case in Fig. 9(b). Of course, the presence of additional atoms on the surface could also affect orientation due to simple steric effects.

Hou et al. [36] observed similar striped HOMO-derived images at a sample bias of -1.8 V on a Si(111)–(7×7) surface (at 78 K). These workers, however, also captured other images at a variety of biases, obtaining different images at each bias used. To explain the observed images, the authors used DFT and found that, depending on adsorption site, the C_{60} molecules adsorb onto the surface with either a single bond or individual atom pointing downwards towards the surface.

Further proof that orientation can be unequivocally assigned on the basis of high-resolution STM images has been provided by Schull et al. [37]. This work shows that long-range orientational ordering of C_{60} molecules adsorbed onto a Au(111) substrate can produce a (7×7) superstructure of adsobates in which each C_{60} has a slightly different orientation, as shown in Fig. 10. This image, recorded at a sample bias of 1.5 V, corresponds to visualising LUMO orbitals and can be reproduced quite easily by imaging the T_{1u} orbitals of C_{60}.

Other workers have realised that the charge state of a C_{60} molecule has important implications with regards electron-vibration interactions and have actively sought to use STM to study the effects of doping. Of particular merit is the work of Crommie and co-workers who, in a series of papers [30, 5, 38, 39], have recorded some very intriguing images and spectra of a series of doped C_{60} molecules. In one experiment [on Ag(111)], these workers

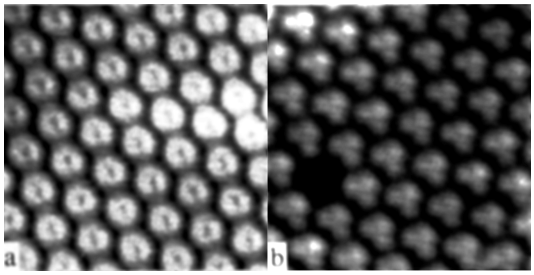

Fig. 8 STM images of a C_{60} monolayer on Cu(111) showing intramolecular detail. (a) images the HOMO (sample bias −2 V) and (b), the LUMO (at +2 V). Reprinted figure with permission from K Motai, T Hashizume, H Shinohara, Y Saito, HW Pickering, Y Nishina and T Sakurai, Jpn. J. Appl. Phys. **32**(3B), L450 (1993) [33]. Copyright (1993) by the Japan Society of Applied Physics.

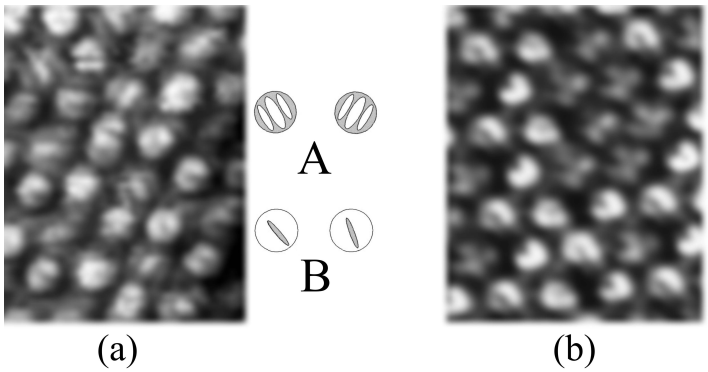

Fig. 9 STM images of C_{60} on a Si(111)–$\sqrt{3} \times \sqrt{3}$–Ag surface at 60 K and sample bias −2 V. (a) shows the undoped monolayer which consists of molecules presenting two different kinds of striped image, labelled A and B. In (b), a K-doped monolayer is imaged, which results in a completely different set of images; bright 'U' and dim 'X' shaped molecules now dominate. Reprinted figure with permission K Tsuchie, T Nago and S Hasegawa, Phys. Rev B **60**, 11131 (1999) [35]. Copyright (1999) by the American Physical Society.

Fig. 10 Low temperature STM image of C_{60} on Au(111) recorded using a bias of 1.5 V. This excerpt, from the original image of a (7×7) superstructure, shows a strip of 8 molecules in which the orientation changes progressively from left to right. Reprinted figure with permission from G Schull and R Berndt, Phys. Rev. Lett. **99**, 226105 (2007) [37]. Copyright (2007) by the American Physical Society.

were able to use the STM tip to progressively attach/detach potassium atoms to individual C_{60} molecules and subsequently record the scanning tunnelling spectroscopy data shown in Fig. 7. In a later work [5], they studied an insulating phase K_4C_{60} and compared it to a conducting layer K_3C_{60}. For small biases, the images of the former are shown in Fig. 11. The authors argue that as the images shown in Fig. 11 are different from each other, there must be a JT effect is present in the doped layer. However, as doping fills the LUMO of C_{60}, we would expect the images to derive from the T_{1u} orbitals, and, as we show later, it is possible to obtain identical images to those shown provided we take certain combinations of the molecular orbitals. The reasons why those particular combinations must be made could be due to the JT effect. However, it could also be due to a surface and/or monolayer interaction or, indeed, some other perturbation. We do not believe that the experiments made to date provide concrete proof that it is possible to directly observe the JT effect in STM images. This is a subject we will return to later. First, though, we will look at a simple way of modelling STM images using molecular orbitals.

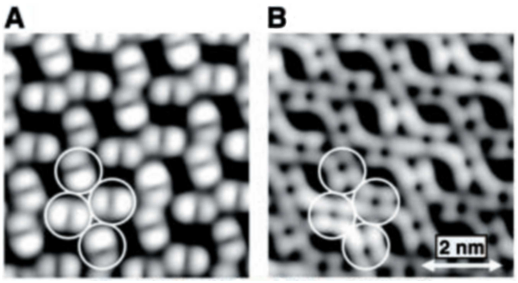

Fig. 11 STM images of K_4C_{60} on Au(111) at small biases (A: −0.1 V and B: +0.1 V). Reprinted figure with permission from A Wachiwiak, R Yamachika, KH Khoo, Y Wang, M Grobis, DH Lee, SG Louie and MF Crommie, Science **310**, 468 (2005) [5]. Copyright (2005) by The American Association for the Advancement of Science.

4 STM simulations and comparison with experiment

We will base our simulations on a simple Hückel molecular orbital (HMO) picture of C_{60}. This approach may not embody the rigour inherent in more sophisticated methods of calculation, such as DFT, but is capable of demonstrating the underlying physical principles without incurring the additional computational cost of methods such as DFT. Where appropriate, we will make comparisons with other theoretical results in the literature, most notably DFT, in order to note similarities or discrepancies.

4.1 Hückel molecular orbital theory for C_{60}

The starting point for our simulations is the analytical treatment of the HMO problem for C_{60} as given by Deng and Yang [40]. These workers used group-theoretic techniques to reduce the 60×60 Hückel Hamiltonian for C_{60} to ten 6×6 sub-matrices, each describable in terms of their parity, p ($= \pm 1$), and an angular momentum-type quantum number, m ($= 0, \pm 1, \pm 2$). The net result is that the form of the HMOs belonging to any particular irrep can be found in terms of 6 constants.

Deng and Yang [40] tabulate expressions for the HMOs that are appropriate to the case where single and double carbon-carbon bonds are equivalent (in the sense that their respective resonance integrals β_s and β_d are equal). However, the theory is sufficient to allow easy extension to a picture in which $\beta_s \neq \beta_d$. To this end, the authors introduce a parameter $\alpha = -\beta_s$ which requires that $\beta_d = \alpha - 2$. In an earlier work [41], we introduced a similar parameter to account for this bond 'alternation', as it is often termed, $\tau = \beta_d/\beta_s$. Thus, the two treatments are related by

$$\alpha = 2\,(1+\tau)^{-1} \ , \tag{7}$$

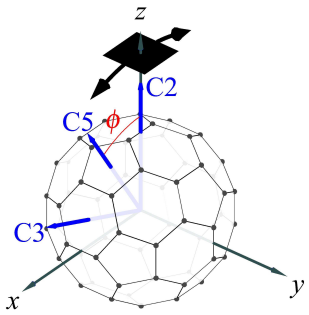

Fig. 12 Definition of the molecular axes and angle ϕ needed to orient the molecule towards the viewing plane (black square).

with the simple, equal-bond picture corresponding to $\alpha = \tau = 1$. In [41], the value $\tau = 1.433$ was derived in order to explain the experimentally observed bond alternation of $r(\mathrm{C}=\mathrm{C}) = 1.391$ Å and $r(\mathrm{C}-\mathrm{C}) = 1.455$ Å. This implies $\alpha = 0.8220$, which is the value of α that we will use when generating our images.

We are interested in generating simple pictures of the molecular orbitals. To do this, we form the required combinations of the sixty radially disposed $2p$ orbitals localized at the carbon nuclei in C_{60}. We assume that the wave functions drop off as e^{-kr}, where, for hydrogen-like atoms, $k = Z_{\mathrm{eff}}/2a_0$, with Z_{eff} the effective nuclear charge and a_0 the Bohr radius. In keeping with our simple approach, we take the effective nuclear charge to be 3.14, as determined by Clementi and Raimondi [42], corresponding to $k \approx 3.0$.

We take our standard molecular axes to pass through the centres of a set of orthogonal carbon-carbon double bonds in the manner shown in Fig. 12. We then set up a fixed 'viewing plane' at a given distance away from the centre of the molecule, as shown Fig. 12. Rotation of the molecule around the y-axis by the correct amount then presents the desired face to the STM tip. Alternatively, we could consider moving the viewing plane in the opposite direction by an equivalent amount. Three important axes are highlighted, each labelled according to the symmetry type: C2 images the molecule when a double bond is pointing downwards towards the surface, whilst C5 ($\phi = 31.72°$) and C3 ($\phi = 69.09°$) present pentagonal and hexagonal faces for viewing. Note, however, that we can also view in this way the two other important orientations, namely over a single bond and an individual atom.

If the orbitals within each irrep are degenerate, then the sums of the squares of the electron densities for the LUMO (T_{1u}) and HOMO (H_u) have the appearances given in Fig. 13 (also see Fig. 2 for the shape of one of the components of the T_{1u} irrep). For neutral C_{60} this means that the filled orbitals are characterised by electrons being localised near the C=C bonds and so these bonds should be prominent at negative STM biases. On the other hand, at positive bias electrons should, at least initially, tunnel into the regions of space associated with the LUMO. In such images, the pentagonal faces (i.e. the C−C single bonds) will appear 'bright'.

4.2 Simulating STM images

In common with most workers, we use the simple tunnelling theory developed by Tersoff and Hamann [43] to provide the final link between the available orbitals and predicted STM image. Their work, which by their own admission contains many approximations, suggests that the tunnelling current I measured during STM is such that

$$I \propto \sum_{\nu} |\psi_{\nu}(\mathbf{r}_0)|^2 \delta(E_{\nu} - E_F) \, , \tag{8}$$

where ψ_{ν} is the wave function of a surface state of energy E_{ν}, $\mathbf{r}_0$ determines the position of the STM tip, E_F is the Fermi energy and ν runs over all the available surface states. In imaging the LUMO, therefore, we assume that sufficient positive bias is applied to the surface so that

$$I_{\mathrm{LUMO}}(\mathbf{r}_0) \propto \rho_{\mathrm{LUMO}}(\mathbf{r}_0) = \sum_{\alpha=x,y,z} |T_{1u\alpha}(\mathbf{r}_0)|^2 \, , \tag{9}$$

where $\rho_{\mathrm{LUMO}}(\mathbf{r}_0)$ is the electron density evaluated at $\mathbf{r}_0$, which is some position vector located within the viewing plane shown in Fig. 12. It is a simple matter to evaluate this expression in a given plane and hence generate a 'constant height' STM image. It is also relatively easy to extend the calculations to create plots which show the tip height required to maintain a constant tunnelling current, i.e. to produce 'constant current' simulations.

Of course, Eq. (9), and its obvious extension to the negative bias case involving $\sum_{\alpha} |H_{u\alpha}(\mathbf{r}_0)|^2$, would only be appropriate if all the orbitals involved are degenerate. Thus, we can use the the density functions shown in

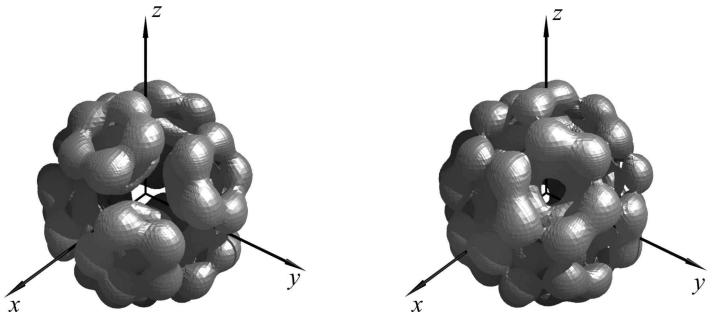

(a) T_{1u} LUMO (b) H_u HOMO

Fig. 13 Isoelectronic density surfaces for (a), the LUMO ($\rho = 0.0050\, e\,\mathrm{Å}^{-3}$) and (b), the HOMO ($\rho = 0.0083\, e\,\mathrm{Å}^{-3}$) in the case when orbital degeneracy is present.

Figs. 13(a) and 13(b) to simulate simple constant height STM images for this degenerate case. Some specific results are shown in Fig. 14.

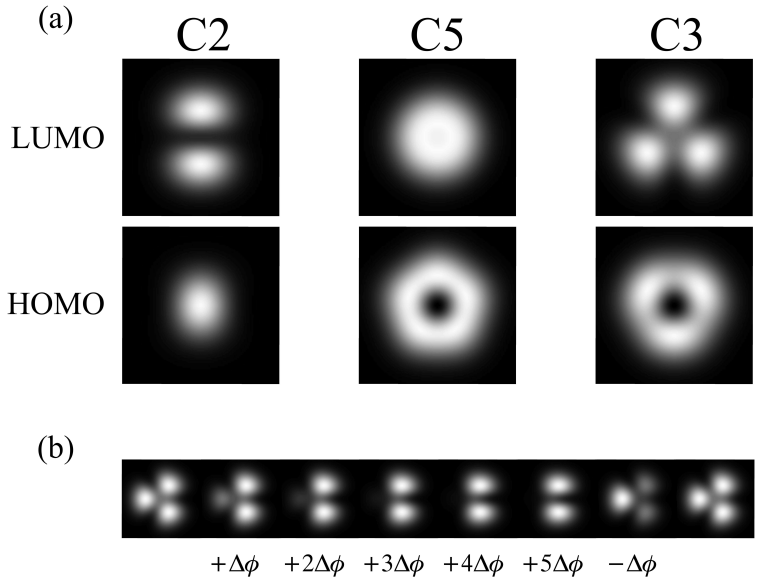

Fig. 14 Simulated, constant-height STM images of C_{60}. In (a), we show the expected appearance of the LUMO and HOMO orbitals when viewed along specific axes (each image is $10\times10\text{Å}^2$). (b) shows a simulation of the orientational effect shown in Fig. 10. The starting orientation corresponds to $\phi = 69.09°$. Additional rotation of $\Delta\phi \simeq 2.6°$ is subsequently added up to a critical rotation after which the subsequent molecules return to orientations close to the original one.

Although simple, some of these simulations bear a strong resemblance to real STM images observed experimentally. Thus, the LUMO and HOMO pictures obtained by viewing along the C3 axis are very similar to those shown in Fig. 8. The LUMO picture viewed along the C2 axis also gives a good match to Fig. 11(A). Fig. 14(b) also shows that we can account for the long-range ordering observed by Schull et al. depicted in Fig. 10. However, it is clear that the six images shown in Fig. 14(a) do not account for all the different STM features that have been observed.

One simple extension would be to vary the orientation to cover the possibility that adsorption occurs with a low-symmetry axis pointing towards the surface, e.g. a C−C single bond or individual C atom could be prone to the surface. However, the most serious omission is, perhaps, the treatment of the LUMO and HOMO as if they retain their three- and fivefold degeneracies in the adsorbed environment. This is certainly not something that would be expected for C_{60} molecules adsorbed onto a surface.

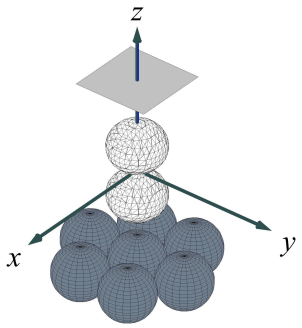

Fig. 15 Diagrammatic representation of the C_{60}-surface system. The surface (dark-grey, close-packed spheres) imposes C_{6v} symmetry on the adsorbed molecule's orbitals (white lobes). Here, a p_z orbital represents the T_{1uz} orbital of C_{60} and the light-grey square is the viewing plane for STM.

4.3 Effects of surface interaction on STM images

Let us suppose that the interaction with the surface is sufficiently strong to cause a loss of degeneracy in the frontier orbitals. Furthermore, assume that the split combinations require different biases for imaging by STM. It is possible that the degeneracy could be lifted completely depending on the symmetry of the surface. Hence, we need a general method of finding which orbitals remain degenerate when exposed to the influence of a surface interaction of a given symmetry.

Here, we describe a simple method of probing degeneracy involving the characters of the orbitals under the group operations associated with the surface symmetry. As (111) surfaces are commonly used in these studies, we shall use as an example a surface symmetry of C_{6v}, as depicted in Fig. 15. We consider the molecule to have a C=C bond pointing towards the surface so that the LUMO basis functions $\{T_{1ux}, T_{1uy}, T_{1uz}\}$ transform as the (x, y, z) themselves or, for illustration purposes, a set (p_x, p_y, p_z) of p-orbitals. Actually, as the T_{1u} orbitals form a basis for the spherical harmonics with angular momentum $L = 1$, this basis can be used whatever orientation is chosen. However, the same cannot be said for the HOMO orbitals as the $L = 5$ harmonics decompose as $T_{1u} \oplus T_{2u} \oplus H_u$ in icosahedral symmetry.

In Fig. 15, we can see that when exposed to an environment of C_{6v} symmetry, the p_z orbital, and hence equivalently the T_{1uz} orbital, will have a character of 1 under any of the group operations of the C_{6v} group and so it transforms as the totally symmetric A_1 irrep. Similarly, we can show that the p_x and p_y orbitals have the same characters and form a basis for the doubly degenerate E_1 irrep. Therefore, this surface interaction will split the LUMO into two parts: a doubly degenerate pair (T_{1ux}, T_{1uy}) and a singly degenerate T_{1uz} orbital. These two sets of orbitals would be expected to produce two distinct STM images (at different biases).

We can repeat the above process for the HOMO orbitals by considering the transformation properties of a set of H_u orbitals. However, as already mentioned, this is more difficult than for the LUMO as these orbitals derive from spherical harmonics with $L = 5$. For any given orientation, an orthog-

onal basis must be found and then the transformation properties examined. Finally, combinations of orbitals must be constructed which have the same transformation characteristics. The overall result is that the fivefold degenerate HOMO splits into three parts: one singly- and two doubly-degenerate combinations. Details of these calculations will be left for a subsequent publication. We do, however, present the resulting STM images to be expected for the configuration currently being considered (i.e. C=C prone to the surface), in Fig. 16.

The simulated STM images in Fig. 16 have been generated in constant current mode using a large tunnelling current in order to give a clear view of the electron densities associated with the images. Note that these 'enhanced' pictures are not realistic simulations of what might be observed in practice. However, they still allow the regions of electron density 'nearest' to the observer to be determined and so it is easy to imagine what the corresponding real STM image might look like. Thus, for the HOMO, two of the combinations (one A, one E) will produce STM images having a striped appearance. These bear a strong resemblance to the experimentally–obtained STM images for 'A' and 'B' species shown in Fig. 9(a), although a direct correspondence is unlikely as our simulated images would be expected to require two different biases for visualisation. The image of the A-type HOMO orbital in Fig. 16 is also interesting because it is identical to a simulation made using DFT by Pascual et al. [44]. In fact, the simple methods used here are able to reproduce all the images obtained using sophisticated DFT calculations in [44] and this fact gives us confidence in the procedures we have used.

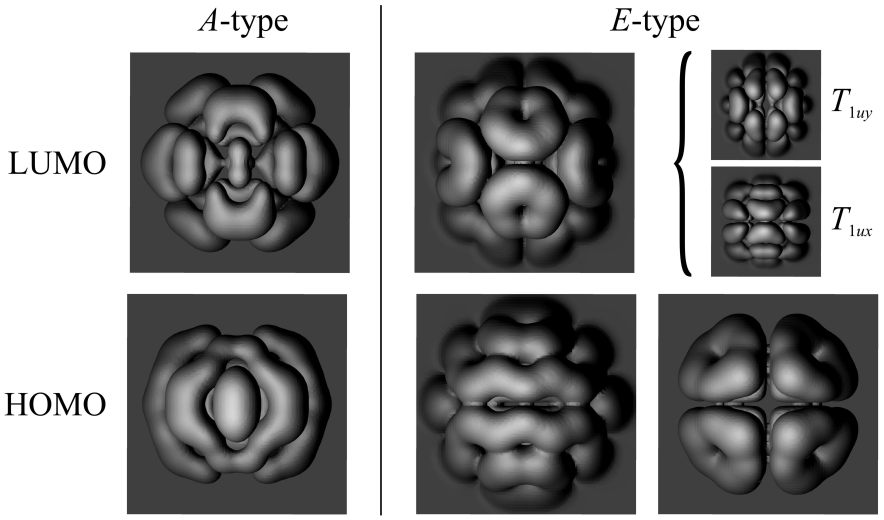

Fig. 16 High-resolution, constant-current simulated STM images for a surface-adsorbed C_{60} molecule. The distribution of the orbitals into doublets and singlets has been induced by a surface with C_{6v} site symmetry.

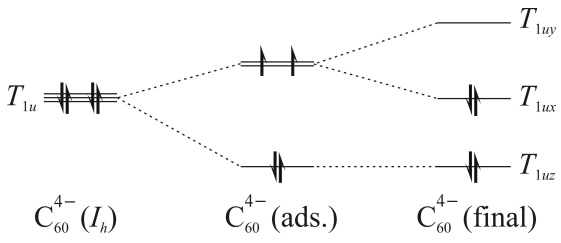

Fig. 17 Illustration of the envisaged energy changes occurring in the LUMO orbitals of K-doped C_{60} (not to scale). The final order is consistent with the STM images of Wachowiak et al. [5].

The LUMO–derived images in Fig. 16 should also be compared with the picture of the T_{1uz} orbital shown in Fig. 2. This orbital becomes the A-type orbital in the presence of the surface (in the $-z$ direction) and as the electron density is held in an equatorial belt lying in the (x, y) plane, the corresponding STM image would be weak. On the other hand, the E-type combination is strong and produces an image very similar to that shown in Fig. 11(A). In Fig. 2, this image corresponds to the sum of the images obtained looking down the x- and y-axes, as highlighted in the upper right part of Fig. 16. In fact, the strong, two-lobed STM image in Fig. 11(A) can be accounted for using the T_{1ux} orbital *alone*. The T_{1uy} orbital, in isolation, produces a weak STM image that matches very closely those seen in Fig. 11(B). The implication of this observation is that the STM images are consistent with a complete loss of degeneracy in the T_{1u} orbitals in the K_4C_{60} monolayer—in other words, the symmetry must be C_{2v} or lower. A schematic representation of the overall energy level scheme is shown in Fig. 17.

If the C_{60} is positioned at a substrate site of C_{6v} symmetry, then the additional lowering of symmetry must be due to an interaction that has been so far neglected. One possibility is that the K^+ counter ions, whose whereabouts are unknown, could reduce the site symmetry beyond that considered. With 4 counter ions to accommodate per C_{60}, it is not difficult to imagine a configuration in which the assumed C_{6v} symmetry could be reduced to C_{2v}, in which degeneracy must be absent. Another possible mechanism, as can be inferred from Fig. 17, is that the doubly occupied E-type orbitals could be responding to a JT interaction of the kind $E \otimes e$. If this were the case, then a strong JT interaction could result in distortion of the molecular cage. However, even though the STM images show remarkable detail, it is very doubtful that the technique is sufficiently detailed enough to resolve the small changes in the shape of the very rigid C_{60} molecule that would accompany JT interaction. The interesting question, considering that STM responds to electronic information and the JT effect affects both vibrational and electronic wave functions, is whether the JT effect can manifest itself in an STM image purely electronically. This is an issue we seek to address in Sect. 5.

In summary, we have seen that using quite primitive methods of visualising molecular orbitals, we can reproduce most of the STM images of C_{60} presented in Sect. 3 without necessarily invoking the JT effect. The images

that have eluded reproduction, interestingly enough, are the ones from C_{60} molecules that have been K-doped. The lack of an ability to describe these images could be due to the JT effect, although the anticipated electron transfer that occurs even in the absence of doping would preclude reservation of the K-doped derivatives for special treatment. It is fairly likely that the added K^+ ions influence the STM image through steric effects and, if these ions are located preferentially on the surface itself, it would be easy to envisage that doping could cause a change in the orientation of the adsorbed C_{60} molecules, as appears to be the case in Fig. 9.

Overall, the evidence to support suggestions that JT effects have been unequivocally observed in STM images [5] seems very thin. One problem with a JT interpretation of these images is that real STM images are influenced by many factors, some of which may be considerably more significant than the rather subtle JT interaction. In contrast, theoretical simulations can be specifically tailored to consider only the effects of a JT interaction, the results of which can be used as a guide to what may appear in actual experiments.

5 Jahn-Teller effects in surface-adsorbed molecules

In this section we shall consider some general aspects of the central problem of interest here. Let us suppose that a JT-active molecule is adsorbed onto a surface in preparation for imaging via STM. In as simple a way as possible, we want to discover what JT-related effects might appear in the captured image under ideal conditions. By 'ideal', we mean ignoring all complications that are present in real images, such as the effect of finite tip size, low resolution, molecule-tip interactions, and even the surface interaction itself. The intention is to concentrate on what arises purely on the basis of the JT effect. Even here, it must again be noted that the very act of performing STM will excite molecules into vibronically-coupled electronic states which may promote dynamical tunneling processes which, in turn, could influence the recorded STM image. Such complications are also ignored here.

5.1 A hypothetical $E \otimes e$ example: X_3

We shall initially dispense with the fullerene molecule itself because of the complicated nature of the JT effects that are possible in this large and highly symmetric molecule (see Sect. 5.2.1). Instead, we consider a simple $E \otimes e$ JT system exemplified by a hypothetical triatomic molecule of the form X_3 of the kind exemplified by Na_3, i.e. one constructed from atoms whose valence electrons reside in s-type atomic orbitals. The molecule is adsorbed onto a similarly hypothetical, atomically flat surface so that each atom is equidistant

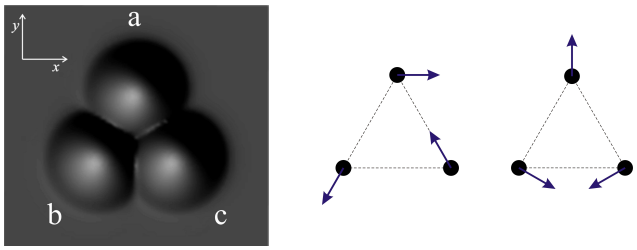

(a) STM simulation (b) Q_x mode (c) Q_y mode

Fig. 18 A simulated, constant-current STM image of a hypothetical X_3 molecule in its high-symmetry D_{3h} configuration is shown in (a). The (x, y)-axes are arranged so that atom 'a' lies on the y-axis and the centre of mass is at the origin. The corresponding degenerate normal modes of vibration are shown in (b) and (c).

from the surface. The surface, therefore, is merely a platform to support the molecule so that it can be imaged via STM. In this way, we attempt to isolate, using simple STM simulations, the features of the image that can be attributed solely to the JT nature of the molecule.

The X_3 constitutes an example of the well-known $E\otimes e$ JT problem, a textbook vibronic coupling problem [45] whose low dimensionality permits the consequences of vibronic interaction to be appreciated using simple pictorial methods. The coupling occurs between doubly degenerate orbitals $\{E_x, E_y\}$ which are occupied by a single electron and have the form

$$\begin{aligned} E_x &= (\psi_b - \psi_c)/\sqrt{2}\,, \\ E_y &= (2\psi_a - \psi_b - \psi_c)/\sqrt{6}\,, \end{aligned} \tag{10}$$

where ψ_a is the s-orbital centred at atom 'a', etc.

In the absence of a JT effect, the atoms will be arranged in the high-symmetry D_{3h} configuration and the electron density sampled will correspond to $|E_x|^2 + |E_y|^2$ for some particular bias. A simulation of the STM image produced by this electron density is shown in Fig. 18, which also shows the doubly-degenerate, in-plane normal modes of vibration of interest

$$\begin{aligned} Q_x &= (2x_a - x_b - \sqrt{3}y_b - x_c + \sqrt{3}y_c)/\sqrt{12}\,, \\ Q_y &= (2y_a + \sqrt{3}x_b - y_b - \sqrt{3}x_c - y_c)/\sqrt{12}\,, \end{aligned} \tag{11}$$

where x_a is the displacement from equilibrium of atom 'a' in the x direction, etc.

The simulation in Fig. 18(a) shows the characteristics that might be expected from this symmetrical arrangement of anti-bonding orbitals, namely, threefold symmetry and nodes between atoms. The next step is to add in a JT effect. In general, the system Hamiltonian can be expressed in the form

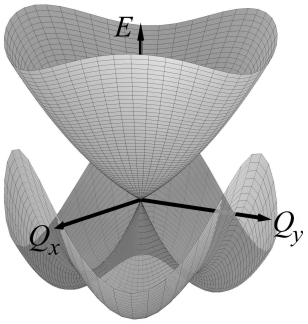

Fig. 19 A graphical depiction of the variation in the energies of the upper (excited) and lower (ground) potential energy surfaces in normal-mode or Q-space for the quadratic $E \otimes e$ JT problem. The origin corresponds to the system in its degenerate, high-symmetry D_{3h} configuration shown in Fig. 18.

$$\mathcal{H} = \mathcal{H}_0 + V_1'\mathcal{H}_1 + V_2'\mathcal{H}_2 \ , \tag{12}$$

where $\mathcal{H}_1$ is the linear JT interaction Hamiltonian involving terms linearly dependent on the normal mode coordinates Q_i, $\mathcal{H}_2$ is the quadratic interaction Hamiltonian dependent on products of the form $Q_i\,Q_j$, $\mathcal{H}_0$ is the Hamiltonian in the absence of coupling and V_i' ($i = 1\,\text{or}\,2$) are dimensionless coupling constants. The explicit form of this Hamiltonian and its solutions are well known [45].

The most obvious effect of the JT interaction is that the electronic orbitals are no longer degenerate, as shown in Q-space in Fig. 19. This implies that we will observe two different STM images at different biases; one from the ground PES and another from the excited PES. Therefore, for imaging purposes, we shall assume that the two biases required are sufficiently large that each electron density can be imaged with negligible interference from the other. Note that this splitting also suggests that STM, if properly calibrated, should be capable of directly measuring energies related to the JT stabilisation energy which, in turn, can be related to coupling strengths.

In Fig. 19, we have illustrated the consequences of a general quadratic JT interaction, viz. the ground PES possesses 3 discrete, isoenergetic minima symmetrically placed around the origin. If the vibronic coupling is very strong, then the system will become trapped in one of these potential minima or 'wells'—i.e. there is a static JT effect. The probability of finding the system in each well will be the same and so 3 equivalent images would be expected to be observed using STM, as indicated in Fig. 20, in which the minima have been arbitrarily associated with an obtuse geometry. Of course, each pair of images are identical but for orientation, and conversion between them corresponds to the unique dynamical motion referred to as pseudorotation [46].

It is clear from Fig. 20 that the presence of a strong JT effect has had a significant effect on the original, unperturbed image shown in Fig. 18(a). The ground state image clearly shows a reduction in symmetry from D_{3h} to C_{2v} and the excited state appears to have an atom missing. This latter facet arises as the 'missing' atom lies on a nodal plane. Fig. 20 also allows

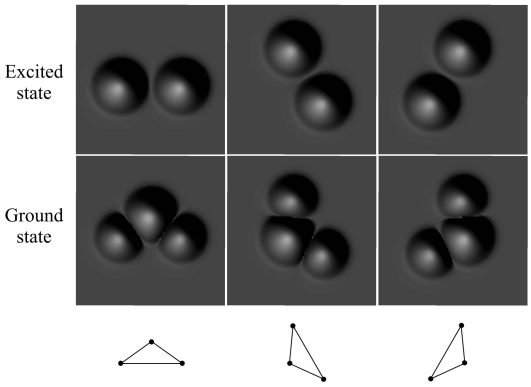

Fig. 20 STM simulation of an X_3 molecule subject to a strong JT effect (to the extent that each configuration has an internal angle of 110°).

us to visualise the effects of accounting for the corrugation of the surface, which has so far been assumed to be flat. Depending on the symmetry of the corrugation (and we notably except C_{6v} and C_{3v} here) the energies of the three configurations shown will become different. Thus, the surface interaction, in the first instance, will have the effect of favouring a subset of the available wells; in other words, the molecule may become locked into one particular well. Or, if two or more wells remain isoenergetic, it may jump between the remaining equivalent configurations. In fact, this is actually the behaviour that we would expect to occur in reality in the 'static' case itself shown in Fig. 20. It is only because we have chosen to consider the vibronic interaction to be arbitrarily large that we have assumed the rate of pseudorotation to be so slow as to be negligible on the time-scale used to capture the STM images. As this time-scale itself is very slow, this suggests that an extremely large vibronic coupling would be required to produce the results shown in Fig. 20.

If we now allow the system to jump between wells, what effect would this have on the image? We can do this by simulating STM images at particular points in Q-space and then taking weighted averages. As we are only interested in first approximations, we can consider two types of behaviour. If the PES is strongly warped (large but finite coupling), then we can expect the system to spend most of its time localised in the wells. Taking the average of the 3 images in Fig. 20, we arrive at the image shown in Fig. 21(b). If the warping is further reduced, so that the PES becomes essentially a flat trough in Q-space, then the system can freely pseudorotate around the trough. Thus, we take an average over 100 equally-spaced points in the trough to obtain the time-average shown in Fig. 21(c).

We can see from Fig. 21 that if the JT effect is dynamic on the time-scale associated with STM capture, then the recorded image takes on a much more symmetrical (D_{3h}) appearance than when the effect was considered static. However, even if the pseudorotation rate is very fast compared to the response rate of the STM imaging apparatus, there will still be residual effects due to

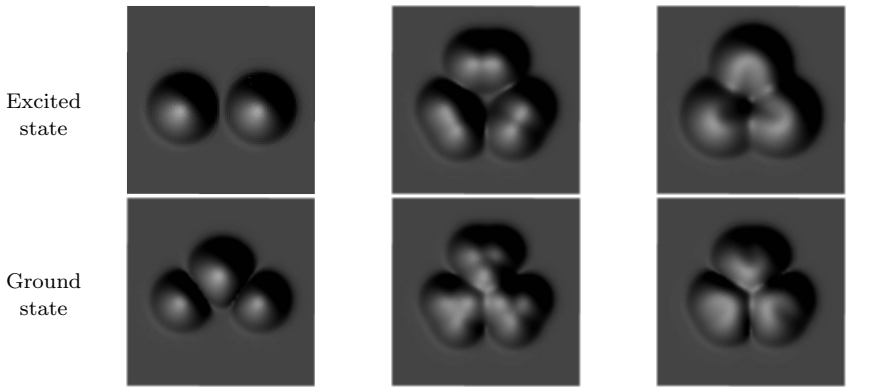

Fig. 21 STM simulations for systems subject to a static vs. dynamic JT effect. The top row corresponds to the excited state and the bottom to the ground state. In (a), infinitely strong coupling locks the molecule into one particular well. Finite but strong coupling (so that the system jumps between 3 wells) is shown in (b). Further reduction in localisation leads to essentially free pseudorotation, producing the time-averaged images in (c).

the JT interaction. The most apparent effect is that the circular orbits traced out by the nuclei are imaged by STM in both the ground and excited states. It is interesting that in the image shown in Fig. 21(c), the ground state electron density appears to be preferentially localised inside the equilateral triangle formed by the average nuclear positions, whereas the converse is true for the excited state.

The occurrence of blurred 'rings of motion' like those shown in Fig. 21(c) in real STM images would provide novel confirmation that pseudorotation is occurring and that the system is actively avoiding the high symmetry configuration. However, this would only be observed if a strong enough JT interaction was present because the diameter of the blurred ring depends on the JT coupling strength; too small a diameter and the vestiges of the JT effect in the image will vanish. This is particularly true for C_{60}, where the molecular bonds are very strong and so the expected displacement of the atoms from their high-symmetry position is very small.

5.2 Jahn-Teller effects in surface-adsorbed fullerenes

The simple $E \otimes e$ JT system discussed in the previous section is useful as it allows one to explore the sort of features that may occur in STM images of JT-active molecules. The same general arguments developed there can also be applied to more complicated systems, such as surface-adsorbed C_{60}. The high symmetry of C_{60} means that a multitude of interesting electron-vibration

coupling systems can be formed when the molecule is doped. A brief review of these systems follows in Sect. 5.2.1. When C_{60} is adsorbed onto a metallic substrate, the most likely doping event to occur will be transferral of electron density into the T_{1u} LUMO. This will be further enhanced if additional doping is carried out using electropositive metals such as potassium. Therefore, we concentrate for the rest of this section on images derived from the LUMO.

We have seen in Sect. 3 that the resolution of the STM images of fullerenes is sufficient to show up some intramolecular detail. However, as the bonding in the fullerene cage is strong, the resolution will not be great enough to show up small changes in shape due to the JT effect. Therefore, we shall ignore the small distortions in our simulations and look for purely electronic effects.

5.2.1 A review of Jahn-Teller effects in discrete fullerene systems

A comprehensive assessment of the JT effect in icosahedral systems may be found in the book by Chancey and O'Brien [47]. Together with the references therein, this book gives a good introduction to the possible JT effects expected in C_{60}. Therefore, only a brief discussion of these systems is given here.

Hückel theory, as we have seen, indicates that the neutral molecule has a fully-filled, fivefold degenerate HOMO of H_u symmetry. The JT effect is therefore absent in the neutral molecule itself. The LUMO, with T_{1u} symmetry, lies about 2 eV higher in energy and is readily available to the molecule leading to a high electron affinity of ~ 2.7 eV [10].

Reduction of C_{60}, most commonly achieved by reaction with highly electropositive Group 1A metals, will thus produce several JT-active species of the form C_{60}^{n-} $(1 \leq n \leq 5)$ possessing a set of partially filled T_{1u} orbitals. The latter can couple to vibrations with h_g symmetry. Single occupation of the LUMO leads to the well-studied $T_{1u} \otimes h_g$ JT system. Higher LUMO occupancies are written in the form $p^n \otimes h$. It is also possible, but more difficult, to oxidise C_{60}. Removal of a single electron (or, equivalently, addition of a single 'hole') produces the C_{60}^{+} ion which is subject to a $H_u \otimes (g \oplus h)$ JT effect. Once again, further doping is possible leading to the general coupling problem $h_u^n \otimes (g \oplus h)$, but the corresponding ions are less likely to be of practical importance due to their difficult preparation and high reactivity.

It quickly becomes clear that there is a rich variety of vibronically coupled systems that may be present in compounds containing doped C_{60}. There are other complications that arise that further complicate the theoretical description of these problems. One such complication is that each of these coupling problems is actually a multimode problem. That is, there are several modes of vibration of C_{60} that can simultaneously couple to the aforementioned electronic states ($6g_g$ and $8h_g$, to be precise). Although this complication can be dealt with (see e.g. [48]), it is often easier to work in terms of a single, effective mode as this is far simpler and reproduces most of the important

aspects of the problem. In fact, in the current context, even the details of some effective mode of vibration are effectively irrelevant as we are ignoring the distortion of the C_{60} cage.

Another complication that warrants mention here is that multiply-doped molecules will be susceptible to electron-electron interactions in addition to vibronic coupling. Once again, this complication can be dealt with, especially if we are interested in numerical results only (see e.g. [49, 50]). Unsurprisingly, in light of the coarseness of our method of simulation, this is another aspect of the problem that will be neglected here. Similarly, we will neglect any intermolecular charge transfer processes and effectively treat the ions as individual entities, with a fixed position on the surface and a fixed charge state.

5.2.2 The LUMO-surface interaction

Let us now concentrate on the T_{1u} LUMO of C_{60}. Referring to Fig. 12, we want to let the molecule have an orientation ϕ with respect to the surface-tip arrangement. Thus, we make new combinations of the basis functions to be associated with laboratory axes (X, Y, Z). The Z-axis will be taken as the normal to the surface, i.e. along the orientation axis and so we take

$$T_{1uZ} = \cos\phi\, T_{1uz} + \sin\phi\, T_{1ux} \ , \tag{13}$$

to be the molecular orbital associated with the Z-axis. For different values of ϕ, the y-axis remains static and so we take the Y-axis to be coincident with its molecular counterpart, so that:

$$\begin{aligned} T_{1uY} &= T_{1uy} \ , \\ T_{1uX} &= -\sin\phi\, T_{1uz} + \cos\phi\, T_{1ux} \ . \end{aligned} \tag{14}$$

If the effect of adsorption is to split the triply degenerate T_{1u} level into a singlet A and doublet E, then we can write the effect of the surface interaction Hamiltonian $\mathcal{H}_{\rm S}$ as

$$\begin{aligned} \mathcal{H}_{\rm S}\, T_{1uX} &= \tfrac{1}{2}\delta\, T_{1uX} \\ \mathcal{H}_{\rm S}\, T_{1uY} &= \tfrac{1}{2}\delta\, T_{1uY} \\ \mathcal{H}_{\rm S}\, T_{1uZ} &= -\delta\, T_{1uZ} \end{aligned} \tag{15}$$

so that the magnitude of the surface splitting is $|\Delta_{\rm S}| = \frac{3}{2}|\delta|$. We also allow δ to be positive or negative to give the required splitting order. Combining Eqs. (13)–(15), the expression for the interaction Hamiltonian in this case, written in the usual $\{T_{1ux}, T_{1uy}, T_{1uz}\}$ electronic basis, is

$$\mathcal{H}_{\rm S} = -\frac{\delta}{4}\begin{pmatrix} 1-3\cos 2\phi & 0 & 3\sin 2\phi \\ 0 & -2 & 0 \\ 3\sin 2\phi & 0 & 1+3\cos 2\phi \end{pmatrix} . \tag{16}$$

It should be noted that this form of $\mathcal{H}_{\rm S}$ will only be true for specific orientations ϕ which result in a symmetry of C_3 or higher, which we expect to correspond to alignment of the Z axis with a C_2, C_5 or C_3 axis. For more general orientations, corresponding to lower symmetries, the T_{1u} level will be split into three singlets and a modified form of $\mathcal{H}_{\rm S}$ will be required involving an additional parameter.

If we treat $\mathcal{H}_{\rm S}$ in Eq. (16) as an additional perturbation to the dynamic JT system, we can find first order corrections to the energies of the wells involved. For orientations away from those which split the LUMO into a doublet and a singlet, this is an approximation. However, we proceed this way to avoid introducing an additional parameter. The results are shown in Fig. 22. In D_{5d} symmetry, for example, the contribution to the energy of well C [which is in the (x, y)-plane] is,

$$\langle E_{\rm C}\rangle = \frac{(1,0,\varphi)\mathcal{H}_{\rm S}(1,0,\varphi)^{\mathsf{T}}}{(1,0,\varphi)(1,0,\varphi)^{\mathsf{T}}} = -\frac{\delta}{4}\left[1+\frac{3}{\sqrt{5}}(\cos 2\phi + 2\sin 2\phi)\right] ,$$

where the label used and its definition follow those used previously[1] [51, 52] and $\varphi = \frac{1}{2}(\sqrt{5}+1)$ is the golden mean.

As we might have expected, the energy of well C is a minimum when the angle ϕ is such that the well is oriented towards the surface. Naturally, the other 5 wells are isoenergetic for this arrangement. The inference is that, if the molecule is experiencing a D_{5d} distortion due to the JT effect and subsequently becomes adsorbed onto a surface with a pentagonal face prone to the surface, then the molecule could become locked into the particular well associated with that face. Or, if $\delta < 0$, the molecule could become preferentially locked in one of the other 5 wells, but pseudorotation between all 5 may also occur. We could use this information to predict what might be seen via STM. However, the resulting images would exhibit fivefold symmetry.

With Fig. 11 in mind, in which twofold symmetry is apparent, we consider instead the case when $\phi = 0$ and the molecule is adsorbed with a C=C bond prone to the surface. The combinations of the wells that need to be considered are apparent from Fig. 22. For example, for a D_{2h}-distorted molecule, there are two preferred configurations. One possibility is that when $\delta > 0$, well A, with electronic state T_{1uz}, has the lowest energy; the other is that wells N ($\sim T_{1uy}$) and O ($\sim T_{1ux}$) form a degenerate pair (i.e. when $\delta < 0$). We do not need to simulate pictures for these cases as they would be virtually indistinguishable from those in the upper part of Fig. 16. The latter scenario

[1] The electronic states for the D_{2h} wells in [52] apply to the $(h_u)^2 \otimes h_g$ JT system, as is appropriate for C_{60}^{2+} ions. Hence, they involve a 10-dimensional electronic basis $\{T_{1g}, T_{2g}, G_g\}$. For use here, only the T_1 part is required.

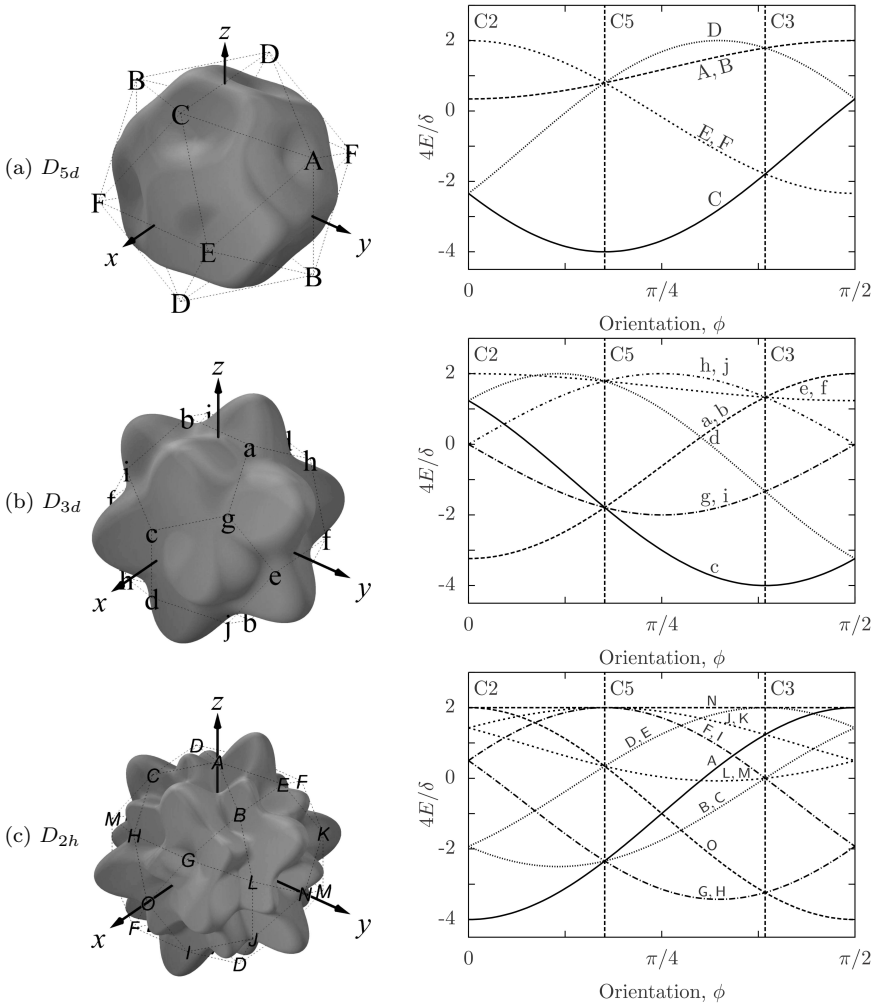

Fig. 22 Pictorial representations of some of the potential wells of various symmetry appropriate to molecules with I_h symmetry. The labels used to identify the potential minima match those used in earlier work [51, 52]. The graphs on the right show the corresponding surface-induced splitting of the wells. As used in Fig. 12, ϕ specifies the angle at which the surface is oriented with respect to the wells.

is the most interesting: if the system was pseudorotating between wells N and O, then we could generate a ground state image to match the negative bias result in Fig. 11. The positive bias image requires knowledge of the excited electronic states, which requires further work that will be left for another publication.

Now consider a D_{5d}-distorted system. We can see from Fig. 22(a) that wells C and D are related to each other by a C_2 rotation about the z-axis.

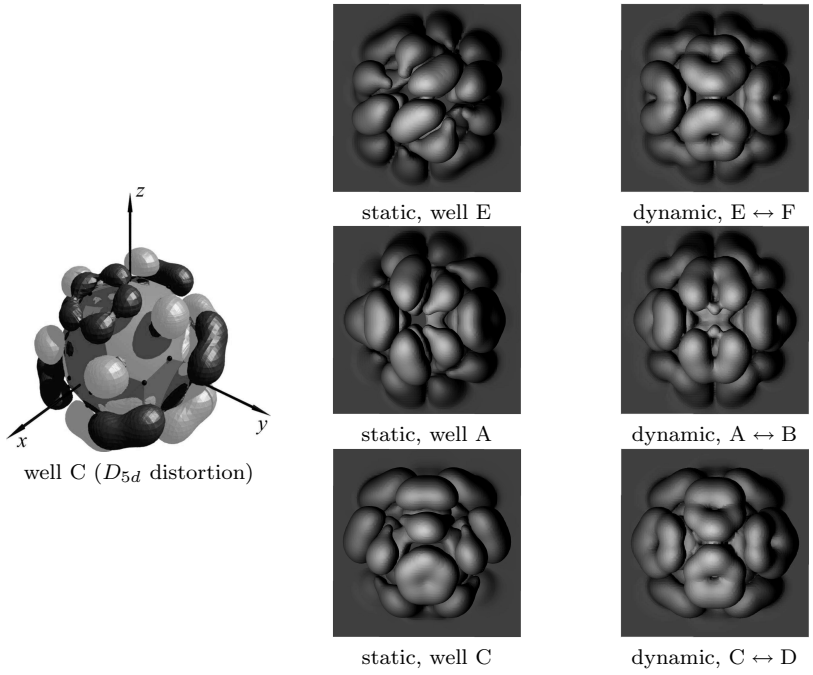

Fig. 23 Plot to show the electronic orbital associated with a D_{5d} minimum (well C). Light-grey lobes represent wave functions with a positive polarity. The adjacent STM simulations show the images expected for the different cases discussed in the text, as viewed along the z-axis.

As we are viewing the molecule along this axis, these two wells will appear identical to each other but inverted. The same applies to the other pairs (A, B) and (E, F). Therefore, we only need to simulate one of each degenerate pair, plus the time-average that would result if the system hopped from one of the wells to its 'twin'. For brevity, let us denote pseudorotation or hopping between two or more wells using the notation A↔B. We collect the resulting images in Fig. 23, together with a picture of the electron distribution associated with a single well (well C). Comparing these simulations with Fig. 16, we see that two of the pseudorotating pairs, C↔D and E↔F, produce images that match the double-lobe negative-bias image shown in Fig. 11. Interestingly, the other pair, A↔B, produces an image very similar to the fourfold symmetric positive-bias image in Fig. 11.

However, the (A, B) pair cannot be directly responsible for producing this image in the real STM data. This is because the states derived from combinations of the wells are all part of the ground electronic state and, as Fig. 11 images C_{60}^{4-} ions, these combinations must correspond to filled states. As already mentioned, further consideration of the excited state manifold is required in order to explain the positive bias images.

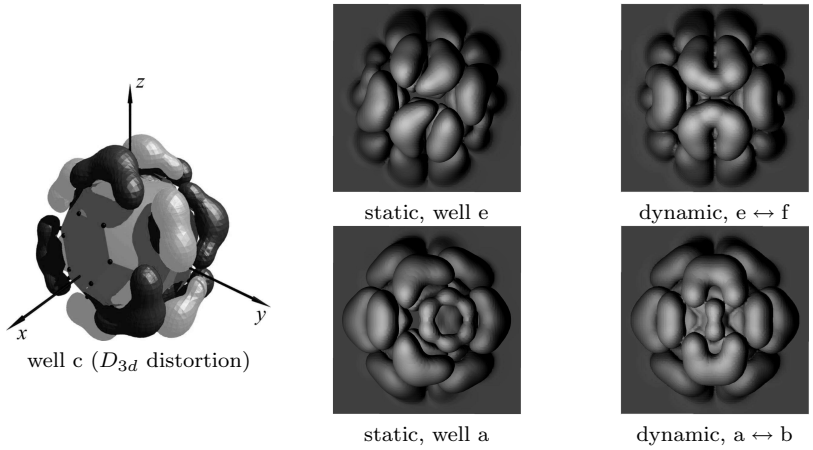

Fig. 24 As for Fig. 23, but illustrating the images produced by D_{3d}-distorted molecules.

Finally we consider the case of D_{3d}-distorted ions. Using Fig. 22 as a guide, we consider the well pairs (a, b) and (e, f) and make comparable simulations, as shown in Fig. 24. These pairs were chosen because they correspond to the lowest and highest energies (depending on δ). The simulated images in this case very closely match those in Fig. 16 and, therefore, the images obtained assuming the presence of D_{2h} wells.

The overall conclusion is that it is possible to generate STM simulations of features that have been found in real images starting from molecules that are D_{2h}, D_{5d} or D_{3d} distorted. If a particular type of distortion is chosen, then there are always several ways in which that distortion can be applied to C_{60}. One cannot simply pick one particular distorted form; rather, it is necessary to look for other forms that are equal in energy (even if adsorbed onto a surface) and to then account for interconversion by hopping or pseudorotation, as this is likely to be fast on the STM time-scale.

6 Summary and conclusions

It is undoubtedly an exciting proposition to study vibronically coupled molecules at the molecular level using tunnelling microscopy. In this article, we have attempted to draw attention to the many complications that may influence the appearance and interpretation of the images obtained via STM. We have used a simple $E \otimes e$ system to illustrate what might be visible in ideal circumstances, but our main goal has been to simulate what might be observed when C_{60} molecules are imaged. C_{60} molecules are an especially exciting choice of JT system to study using STM because they are relatively large and highly symmetric. Thus, the doped molecules can display a diverse

and rich variety of JT effects and the resulting distortion has a reasonable chance of making itself apparent in the STM image.

We have tried to distinguish between static and dynamic JT effects. However, the difference between these two regimes is really the time-scale with which the molecule is observed. Data capture in STM is undoubtedly 'slow' and this must be seen as one drawback of this method of study. For a JT-active molecule, there is usually a set of distorted configurations that are isoenergetic (or, perhaps, nearly isoenergetic if the host surface has a weak effect on them) and interconversion between them is to be expected. The interconversion rate is expected to be rapid on the STM time-scale and so its effect on the recorded STM image needs to be addressed.

In C_{60}, the intramolecular bonds are strong and it is thought that the distortion caused by the JT effect will be small. If this is the case, then current STM equipment may not have the resolution required to directly detect the change in shape that results. In any case, as outlined above, the dynamic nature of the JT effect may produce a time-averaged shape that is essentially icosahedral. Our best hope seems to be that the electronic components of the vibronic states alone will provide sufficient evidence for unequivocal identification of the JT effect present.

To this end, we have used the electronic states associated with the ground state wells of D_{5d}, D_{3d} and D_{2h} symmetry to provide a first attempt at simulating what might be observed via STM. In each case, we can produce images to match those observed by Wachowiak et al. [5]. We can also do this without invoking a JT effect, provided we assume that the surface or some other interaction (e.g. neighbouring C_{60} molecules) splits the T_{1u} orbitals. Therefore, we do not think that the STM results currently available in the public domain constitute conclusive evidence to justify claims that the JT effect has been observed using this technique. However, this does not preclude the possibility that features have been observed which are, in fact, due to the JT effect—simply that the case is not proven. A more thorough investigation is called for which examines both ground and excited states and takes into account coupling strengths and the corresponding time-scales.

There is still much work to be done if we are to fully understand the complicated interplay between the JT effect, surface interaction and the dynamic processes that are inevitably present. Further experimental work will doubtless follow, and has the potential to reveal much. Consequently, it is essential that theoretical work keeps apace so that the information revealed is correctly interpreted.

Acknowledgments

IDH and JLD gratefully acknowledge funding for this work from EPSRC (UK) [Grant number EP/E030106/1].

References

1. G. Binnig, H. Rohrer, Helv. Phys. Acta **55**(6), 726 (1982)
2. G.K. Binnig, H. Rohrer, IBM Journal of Research and Development **30**(4), 355 (1986). [Reprinted, ibid. **44**(1), 279 (2000)]
3. C. Bai, *Scanning Tunneling Microscopy and Its Application*, 2nd edn. (Springer, 2000)
4. C.J. Chen, *Introduction to Scanning Tunneling Microscopy*, 2nd edn. (Oxford University Press, New York, 2008)
5. A. Wachowiak, R. Yamachika, K.H. Khoo, Y. Wang, M. Grobis, D.H. Lee, S.G. Louie, M.F. Crommie, Science **310**(5747), 468 (2005)
6. A.F. Hebard, M.J. Rosseinsky, R.C. Haddon, D.W. Murphy, S.H. Glarum, T.T.M. Palstra, A.P. Ramirez, A.R. Kortan, Nature **350**, 600 (1991)
7. M.J. Rosseinsky, A.P. Ramirez, S.H. Glarum, D.W. Murphy, R.C. Haddon, A.F. Hebard, T.T.M. Palstra, A.R. Kortan, S.M. Zahurak, A.V. Makhija, Phys. Rev. Lett **66**, 2830 (1991)
8. O. Gunnarsson, *Alkali-Doped Fullerides: Narrow-Band Solids with Unusual Properties* (World Scientific, Singapore, 2004)
9. O. Gunnarsson, Rev. Mod. Phys. **69**, 575 (1997)
10. X.B. Wang, C.F. Ding, L.S. Wang, J. Chem. Phys. **110**(17), 8217 (1999)
11. U. Kemiktarak, T. Ndukum, K.C. Schwab, K.L. Ekinci, Nature **450**(7166), 85 (2007)
12. F. Besenbacher, E. Lægsgaard, I. Stensgaard, Mater. Today **8**(5), 26 (2005)
13. J. Repp, G. Meyer, K.H. Rieder, P. Hyldgaard, Phys. Rev. Lett. **91**(20), 206102 (2003)
14. L.L. Wang, H.P. Cheng, Phys. Rev. B **69**, 045404 (2004)
15. E. Burstein, S.C. Erwin, M.Y. Jiang, R.P. Messmer, Phys. Scr. **T42**, 207 (1992)
16. S. Modesti, S. Cerasari, P. Rudolf, Phys. Rev. Lett. **71**, 2469 (1993)
17. L.H. Tjeng, R. Hesper, A.C.L. Heessels, A. Heeres, H.T. Jonkman, G.A. Sawatzky, Solid State Commun. **103**, 31 (1997)
18. B.W. Hoogenboom, R. Hesper, L.H. Tjeng, G.A. Sawatzky, Phys. Rev. B **57**, 11939 (1998)
19. C. Cepek, M. Sancrotti, T. Greber, J. Osterwalder, Surf. Sci. **454**, 467 (2000)
20. R. Nouchi, I. Kanno, J. Appl. Phys. **97**, 103716 (2005)
21. M. Casarin, D. Forrer, T. Orzali, M. Petukhov, M. Sambi, E. Tondello, A. Vittadini, J. Phys. Chem. C **111**, 9365 (2007)
22. T. Kobayashi, C. Tindall, O. Takaoka, Y. Hasegawa, T. Sakurai, J. Korean Phys. Soc. **31**, S5 S8 (1997)
23. E. Bertel, G. Rosina, F.P. Netzer, Surf. Sci. **172**, L515 (1986)
24. A. Sellidj, B.E. Koel, J. Phys. Chem. **97**, 10076 (1993)
25. S. Suto, K. Sakamoto, T. Wakita, C.W. Hu, A. Kasuya, Phys. Rev. B **56**, 7439 (1997)
26. D.R. Lide. CRC Handbook of Chemistry and Physics, 88th Edition online. Table **12**-114 (2008). URL http://www.hbcpnetbase.com/. Accessed 18 December 2008
27. T. Frederiksen, K.J. Franke, A. Arnau, G. Schulze, J.I. Pascual, N. Lorente, Phys. Rev. B **78**, 233401 (2008)
28. A.M. Bradshaw, N.V. Richardson, Pure & Appl. Chem. **68**, 457 (1996)
29. M. Wierzbowska, M. Luders, E. Tosatti, J. Phys. B-At. Mol. Opt. Phys. **37**, 2685 (2004)
30. R. Yamachika, M. Grobis, A. Wachowiak, M.F. Crommie, Science **304**, 281 (2004)
31. R.J. Wilson, G. Meijer, D.S. Bethune, R.D. Johnson, D.D. Chambliss, M.S. de Vries, H.E. Hunziker, H.R. Wendt, Nature **348**, 621 (1990)
32. T. Sakurai, X. Wang, Q.K. Xue, Y. Hasegawa, T. Hashizume, H. Shinohara, Prog. Surf. Sci. **51**, 263 (1996)
33. K. Motai, T. Hashizume, H. Shinohara, Y. Saito, H.W. Pickering, Y. Nishina, T. Sakurai, Jpn. J. Appl. Phys. **32**, L450 (1993)
34. Y. Maruyama, K. Ohno, Y. Kawazoe, Phys. Rev. B **52**, 2070 (1995)
35. K. Tsuchie, T. Nagao, S. Hasegawa, Phys. Rev. B **60**, 11131 (1999)

36. J.G. Hou, Y. Jinlong, W. Haiqian, L. Qunxiang, Z. Changgan, L. Hai, B. Wang, D.M. Chen, Q. Zhu, Phys. Rev. Lett. **83**, 3001 (1999)
37. G. Schull, R. Berndt, Phys. Rev. Lett. **99**(22), 226105 (2007)
38. Y. Wang, R. Yamachika, A. Wachowiak, M. Grobis, K. Khoo, D.H. Lee, S.G. Louie, M.F. Crommie, Phys. Rev. Lett. **99**(8), 086402 (2007)
39. Y. Wang, R. Yamachika, A. Wachowiak, M. Grobis, M.F. Crommie, Nature Mater. **7**, 194 (2008)
40. Y. Deng, C.N. Yang, Phys. Lett. A **170**(2), 116 (1992)
41. I.D. Hands, J.L. Dunn, C.A. Bates, V.Z. Polinger, Chem. Phys. **278**(1), 41 (2002)
42. E. Clementi, D.L. Raimondi, J. Chem. Phys. **38**(11), 2686 (1963)
43. J. Tersoff, D.R. Hamann, Phys. Rev. B **31**, 805 (1985)
44. J.I. Pascual, J. Gómez-Herrero, C. Rogero, A.M. Baró, D. Sánchez-Portal, E. Artacho, P. Ordejón, J.M. Soler, Chem. Phys. Lett. **321**, 78 (2000)
45. I.B. Bersuker, V.Z. Polinger, *Vibronic Interactions in Molecules and Crystals* (Springer-Verlag, Heidleberg, 1989)
46. I.B. Bersuker, *The Jahn-Teller Effect* (Cambridge UP, 2006)
47. C.C. Chancey, M.C.M. O'Brien, *The Jahn-Teller Effect in C_{60} and other Icosahedral Complexes* (Princeton University Press, Princeton, 1997)
48. I.D. Hands, J.L. Dunn, W.A. Diery, C.A. Bates, Phys. Rev. B **73**, 115435 (2006)
49. I.D. Hands, W.A. Diery, J.L. Dunn, C.A. Bates, Phys. Rev. B **76**, 085426 (2007)
50. L.M. Sindi, I.D. Hands, J.L. Dunn, C.A. Bates, J. Mol. Struct. **838**, 78 (2007)
51. J.L. Dunn, C.A. Bates, Phys. Rev. B **52**, 5996 (1995)
52. I.D. Hands, W.A. Diery, J.L. Dunn, C.A. Bates, J. Mol. Struct. **838**, 66 (2007)